PLASMONIC GOLD NANOPARTICLE AS SURFACE LOADING FOR CARBON

DIOXIDE REDUCTION ON TITANIUM DIOXIDE PHOTOCATALYST WITH

ALUMINIUM OXIDE INTERLAYER

A Thesis

by

XIAOYU ZHENG

Submitted to the Office of Graduate and Professional Studies of
Texas A&M University
in partial fulfillment of the requirements for the degree of

MASTER OF SCIENCE

Chair of Committee,	Ying Li
Committee Members,	George Matt Pharr
	Pao-Tai Lin
Head of Department,	Daniel A McAdams

December 2017

Major Subject: Mechanical Engineering

ABSTRACT

A novel structured gold nano-particles loaded TiO_2 photocatalysts with Al_2O_3 interlayer were prepared. Photocatalytic activities of CO_2 reduction with water were tested to characterize the photocatalysis mechanism of these gold nanoparticles. Atomic layer deposition showed a certain thickness of Al_2O_3 passivation layer coating could improve overall efficiency via suppressing surface recombination. The combined effect of plasmonic NPs and passivation layer dramatically enhanced photoactivity. UV-vis spectrum, XRD, and SEM were used to characterize the catalysts further. FDTD calculation is also included to validate with experimental results. The contribution of different mechanisms of plasmonic metal NPs was evaluated. LSPR-assisted charge separation effect was determined to be the most critical function of gold NPs. Correlation among different functions of gold NPs with contact type and spatial size is also included.

DEDICATION

To my mother, my father, my sister, my grandfather, and my grandmother.

ACKNOWLEDGEMENTS

I would like to thank my friends and colleagues and the department faculty and staff for their help and company, with which I experienced an unforgettable period of time in Texas A&M University.

Thanks to my committee chair and members, Dr. Li, Dr. Pharr, and Dr. Lin for their guidance and support throughout this research.

Finally, thanks to my parents and sister for their support and trust.

CONTRIBUTORS AND FUNDING SOURCES

Contributors

Part 1, faculty committee recognition

This work was supervised by a thesis committee consisting of Professors Ying Li and George Matt Pharr of the Department of Mechanical Engineering and Professor Pao-Tai Lin of the Department of Materials Science and Engineering.

Part 2, student/collaborator contributions

Dr. Huilei Zhao provided the SEM image and UV-vis data in Chapter 3.

All other work conducted for the thesis was completed by the student independently.

Funding Sources

Graduate study was supported by an assistantship from Texas A&M University.

NOMENCLATURE

PNP   Plasmonic Nano-Particle

PD   Photo-Deposition

CB   Conduction Band

VB   Valence Band

SRH   Shockley-Read-Hall process

TABLE OF CONTENTS

LIST OF FIGURES

LIST OF TABLES

CHAPTER I

INTRODUCTION AND LITERATURE REVIEW

In the past few decades, greenhouse gases emission has become an increasingly severe problem. While the emission of greenhouse gases was growing consistently to satisfy the increasing energy and manufacture demands, the recycling capability of greenhouse gases is yet inferior. This mismatch is likely causing accelerated global warming[1]. Accordingly, many research has emerged for the innovation of low carbon emission and greenhouse gas capture technologies to ease this issue.

Among these technologies, photocatalytic reduction of carbon dioxide by water has gained more and more attention as a promising method to simultaneously reduce overmuch carbon dioxide in the atmosphere and convert solar energy into chemical energy [2-6]. Similar to photosynthesis, photocatalytic carbon dioxide reduction can recycle CO_2 in the atmosphere to chemical energy stored compound, mostly hydrocarbon and alcohol. Therefore, it is also named "Artificial Photosynthesis."

Though a great amount of catalyst has been investigated as photocatalysts, TiO_2 is still the most widely used photocatalyst since the initial discovery of photocatalysis phenomena[7]. Regarding CO_2 reduction by water, TiO_2 is widely used for its high chemical and thermal stability, room temperature active, appropriate conducting band and valence band edges, low cost and non-toxicity. However, as a wide band-gap (3.2eV for anatase phase) semiconductor, TiO_2 has poor photoexcitation under visible light irradiation. Only photons with a wavelength shorter than 387.5 nm, which is already in

UV light region, can photo-excite TiO2. Moreover, while reduction of CO_2 molecules is a multi-electron process with a first step requiring very negative potential (-1.90V vs. NHE) [2], TiO_2 has high surface recombination rate and low surface CO_2 adsorption capability, making CO_2 photoreduction kinetically disfavored [6]. Hence, extrinsic doping or loading is often applied in TiO_2 based catalysts in order to enhance the overall performance. Metal doping, e.g. Cu [4], Pt [8], Ag [3, 9], Au[10] and Pd [11], can enhance surface electron-hole pairs separation (Schottky barrier electron trapping, I in Fig. 1) [6], tune the Fermi level of catalysts [12] and extend the lifetime of photoinduced carriers, hence improve CO_2 reduction activity.

Specially, plasmonic metal loading, e.g., Ag [3, 9], Au[10], can introduce additional benefits by plasmonic effect [3, 9]. In short, the plasmonic effect is caused by light-induced surface plasmon response, in which plasmon stands for a quasi-particle arises from the quantization of plasma oscillation. Regarding near-sphere shaped plasmonic NPs (PNPs) which we interested in, the pre-dominating plasmonic mode is Localized Surface Plasmons (LSPs), in which the time-varying electric field induces a collective oscillation of electrons in the conduction band of metal nanoparticles[13]. As the resonant frequency is depended on the physical properties of PNPs, with appropriate choice of the composition, shape, and dimension of PNPs, the resonant frequency can be tuned to the visible light region or IR region. In photocatalysis system, LSPR can generate hot electrons in plasmonic particles via non-radiative damping of plasmon[14], which can thereafter migrate to TiO_2 conduction band if TiO_2 is in electrical contact with plasmonic NPs (II in Fig. 1). In this process, PNPs coupling offers an alternative to

overcome a less energy gap than direct photoexcitation in TiO_2, extending its photo-response to visible or IR region. LSPR can also cause intense localized electric field near metal NP's surface (III in Fig. 1). According to Fermi's golden rule,

$$\Gamma_{i \to f} = \frac{2\pi}{\hbar} |\langle f|H'|i \rangle|^2 \rho$$

in which $\langle f|H'|i \rangle$ is the matrix element of perturbation H', ρ is the density of final states. The enhanced electric field can in turn enhance the photoexcitation rate in semiconductor. Recently, some researchers also reported another mechanism called resonant energy transfer [15], in which plasmons transfer to semiconductor by dipole-dipole interaction without direct contact (IV in Fig. 1). This process requires plasmonic resonant frequency to be close to the bandgap of semiconductor and is generally insignificant for Au/TiO_2 structure[16]. Therefore, dipole-dipole interaction is excluded in the discussion of this thesis as our Au NPs have resonant peak wavelength larger than 500 nm. Beside of these major functions, plasmonic metal NPs can also polarize nonpolar molecules for better adsorption and heat up local environment for higher reaction kinetics[9].
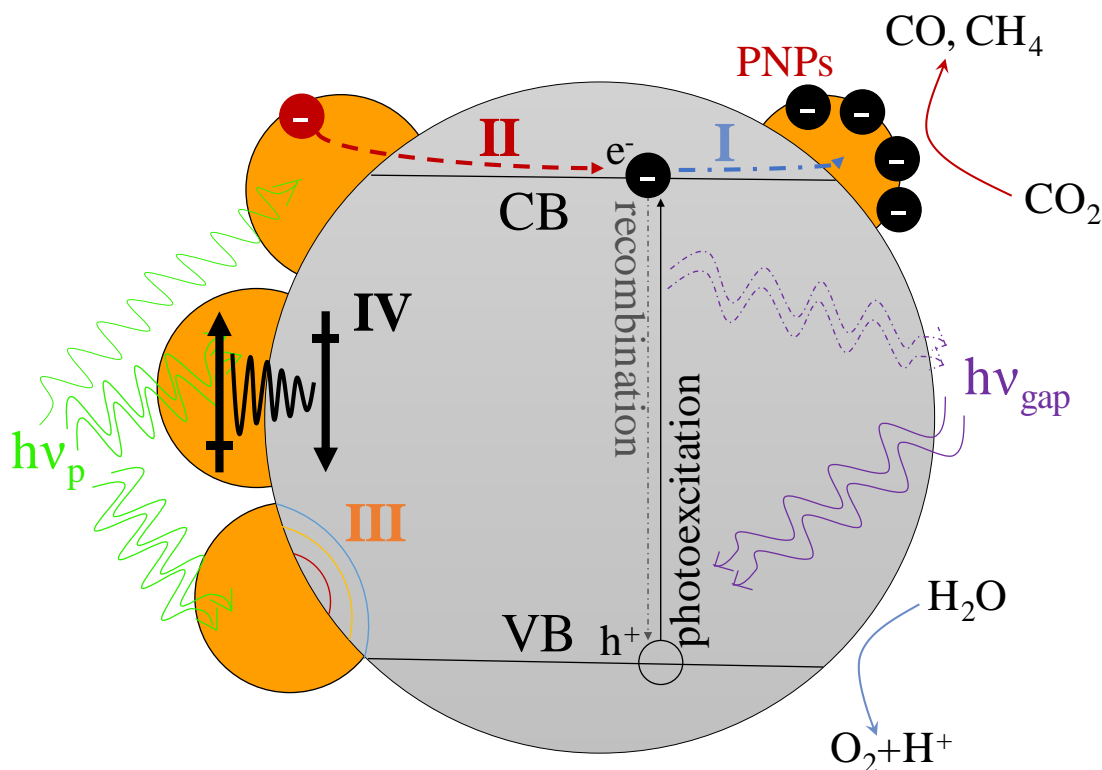
Figure 1 Plasmonic/non-plasmonic effects in photocatalysis

Several pioneer works have been done on PNPs assisted CO_2 reduction by water on TiO_2 based photocatalysts. Hou et al. applied Au NPs to TiO_2 photocatalyst and achieved a 24-fold yield enhancement under 532nm light illumination[17]. They attributed this enhancement to the enhanced electric field and d-band transition in Au. Tu et al. prepared Au@TiO_2 yolk-shell hollow spheres with enhanced CO_2 photoreduction activity[18]. They accounted the promotion effect by the electric field created by Au NPs. Kar et al. grafted Au NPs to short n-type anatase TiO_2 nanotube arrays (TNAs) and detected ten times larger CH_4 yield than pure TNAs[19]. They

attributed the enhancement to an interfacial electric field and charge separation effect. Though the positive effects of attaching plasmonic NPs to TiO_2 for CO_2 photoreduction is recognized, the role of PNPs in photocatalysis system is still not clear for the complex origin of its promotion effect. As stated above, plasmonic NPs has various plasmonic/non-plasmonic effect in a photocatalyst system. Previous works mostly attributed the contribution of plasmonic metals to the electric field or the hot electron injection without rigorous correlation, or solely attribute it to the combined effect of all the effects without quantitative evaluations. However, to design a highly efficient plasmonic photocatalyst, it is necessary to evaluate these effects quantitatively.

In this thesis, an Au NPs/Al_2O_3 atomic interlayer/TiO_2 NP nanostructure is investigated. We applied sodium citrate reduction method[20] to prepare different size gold NPs. We decoupled different effects of Au NPs by manipulating the nanostructure and the light source. Visible light experiments characterized the contribution of hot electron injection. FDTD simulation is also included to support our hypothesis. We clarified the dependence of each effect on PNPs size and contact type, which provides useful guide for plasmonic photocatalyst design.

CHAPTER II

EXPERIMENTAL AND CHARACTERIZATION METHODS

The activity testing procedure and apparatus are similar to our previous work [21]. A schematic for the whole system is shown in Fig. 2. Firstly, 10mg of catalyst was mixed with 1mL DI water. Then the mixture was uniformly dispersed onto a rectangular glass fiber filter ($1*2$ inch^2, pre-calcined) by pipette. After being dried, the glass fiber filter was loaded into a cylindrical quartz tube which has CO_2 inlet and after-reaction gas outlet. The outlet gas was analyzed by a GC-TCD/FID apparatus (Fuel Cell GC-2014ATF, Shimadzu) with thermal conductivity detector (TCD) and methanizer assisted flame ionization detector (FID) equipped, which can detect the concentration of several carbon-containing gas species (including CH_4 and CO). 0.4 L/min gas flow rate was used for 1hr purge, and then 4mL/min flow rate, same as working flow rate, was used for another 1hr purge. Wavelength filters can be applied to the window of Xeon lamp to control the illumination wavelength. Then a 450W Xe lamp (Newport) was turned on as the light source. Light on activity test will last 4 hrs.
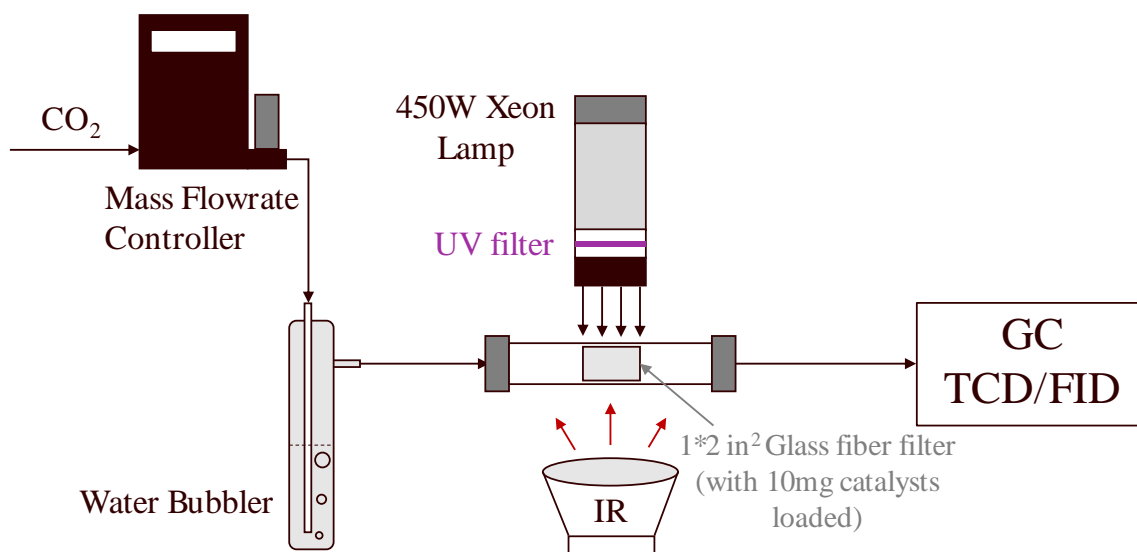
Figure 2 Schematic of experimental set-up for CO_2 photoreduction

Au NPs are prepared by sodium citrate reduction method [20]. In this method, a different molar ratio between Na_3Ct and $HAuCl_4 \cdot 3H_2O$ precursor was used to sustain different pH of the mixture, resulting in different reduction dynamics and Au nanoparticle sizes. Briefly, the desired amount of 0.25mM $HAuCl_4 \cdot 3H_2O$ solution was stirred under oil warm at boiling point. Then sodium citrate solution (with desired Na_3Ct amount) was dropwise added in, forming mixtures with 3.5/7/14:1 Na_3Ct: $HAuCl_4$ molar ratio. The solution was kept at boiling temperature until it reached a wine red color, which should consist of 10/20/30 nm Au nanospheres, respectively, based on the literature. Then desired amount of Au nanospheres suspension was mixed with substrate photocatalyst powder and stirred overnight. The obtained sample was then washed and centrifuged for 5 times and dried to remove precursor contamination. Au content was set

to be 0.5 wt.% for all the catalyst in our experiment based on our own activity test shown in Fig. 3 and literature [22, 23].
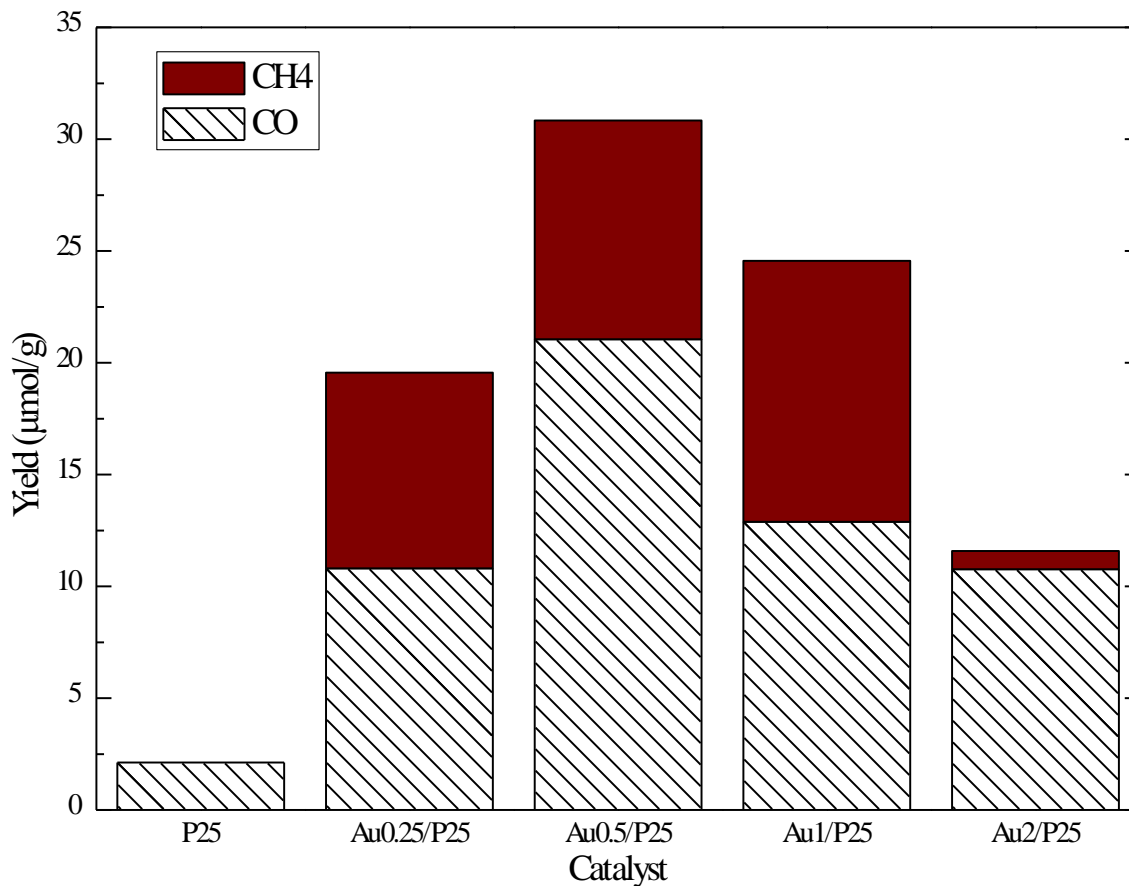
Figure 3 CO₂ reduction activity of photo-deposition photocatalysts

Au/TiO₂ used for weight ratio estimation experiment was prepared by photo-deposition method [24]. In this method, photoexcited electrons were used for in-situ reduction of the gold ion on the semiconductor surface, forming ~5nm small clusters of Au. Briefly, the desired amount of HAuCl₄•3H₂O precursor and P25 was mixed with DI water and hole scavenger to form 50 mL suspension. 2 vol.% methanol was used as the

hole scavenger. Photodeposition was operated under illumination of a 150W UV lamp for 1hr. Then the catalyst was washed, centrifuged and dried overnight.

Atomic layer deposition of Al_2O_3 was applied to prepare substrate catalysts (Al_2O_3/TiO_2). A similar procedure to previous work [21] with minor modification was used. Briefly, a commercial ALD system (Savannah S200, Ultratech) was applied for ALD. Pre-washed P25 powders was used as coating substrate. Trimethylaluminum (TMA, $Al(CH_3)_3$) was used as Al precursor. The reaction chamber was set at 200 °C during the coating. 1/5/20/50 cycle times and 0.1s pulse time was used. For ALD of Al_2O_3, TMA gas firstly reacts with hydroxyl groups on the TiO_2 surface, forming an intermediate surface state with methyl groups exposed and CH_4 exhaust gas. Then H_2O was introduced to react with intermediate states to form another layer of hydroxyl groups, with CH_4 exhaust gas as well. Theoretically, under expo mode with 0.1s pulse time, Al_2O_3 coating will form ~1-angstrom thick layer per cycle. Thus the Al_2O_3 layer formed would be 0.1/0.5/2/5 nm thick, respectively. After the ALD procedure, the Al_2O_3/P25 catalysts were calcined under 450°C for 2hrs to remove contaminants. The as-prepared Al_2O_3/TiO_2 composites are denoted as xAl/TiO_2, where x is the cycle time.

X-ray diffraction (XRD, BRIKER D8) with Cu Kα irradiation at 45 kV and 40 mA diffracted beam monochromator was used to characterize the crystal structures of photocatalysts. A scanning electron microscopy (SEM, JEOL JSM7500F) equipped with a cold cathode UHV field emission conical was applied to obtain the surface morphology. UV-vis diffuse reflectance spectra were obtained via a Hitachi U4100 UV-vis-NIR Spectrophotometer with Praying Mantis accessory.

CHAPTER III

EXPERIMENTAL RESULTS

The crystal structure of photocatalyst samples was characterized by XRD. Fig. 4 shows the XRD pattern of Au(30nm)/P25, Au(10nm)/P25 and Au(10nm)/50Al/P25. From the XRD pattern, we can find that all the samples have TiO_2 (anatase/rutile) peak characteristics with similar intensity to P25. Thus, we can deduce that the XRD signals are originated from P25 in all the photocatalyst samples, while Au NPs and Al_2O_3 coating layer did not show a distinct peak. The above results can be explained by the fact that the amount of Au loading (0.5 wt.%) is too small to form an XRD peak, while the Al_2O_3 coating layer is amorphous.

Figure 4 X-ray diffraction pattern of selected photocatalyst samples
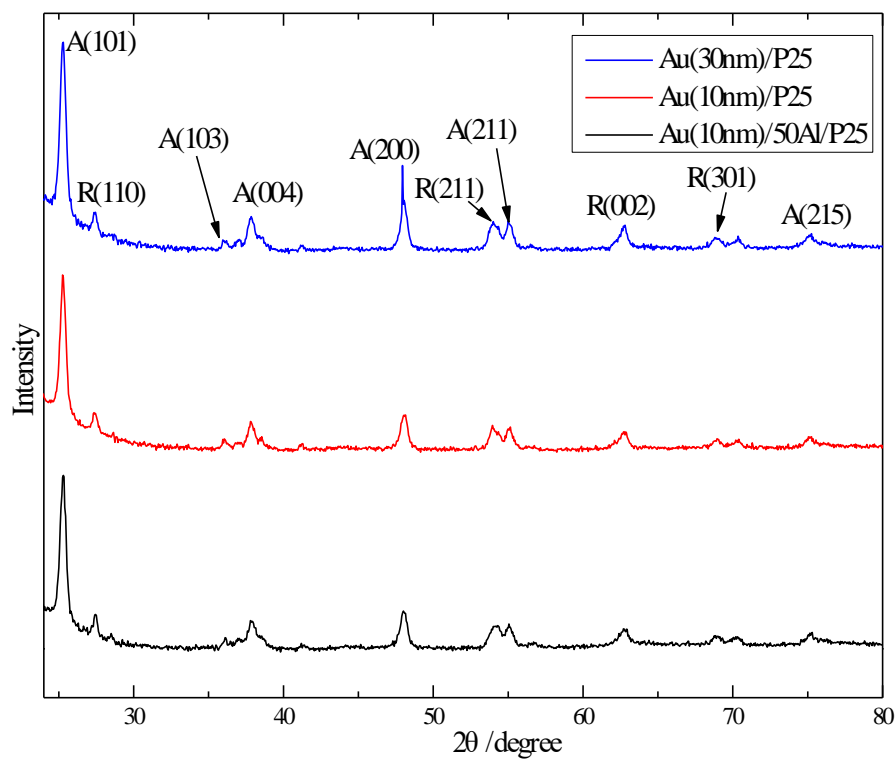
Fig. 5 shows the scanning electron microscope image of Au(20nm)/P25. SEM image of Au/P25 shows that after loading of Au NPs, the catalyst maintained a nano-sized crystal structure with ~20nm size and formed ~1μm agglomerations, which is similar to pristine P25. Therefore, loading of Au NPs does not induce significant change to the morphology of P25 substrate.
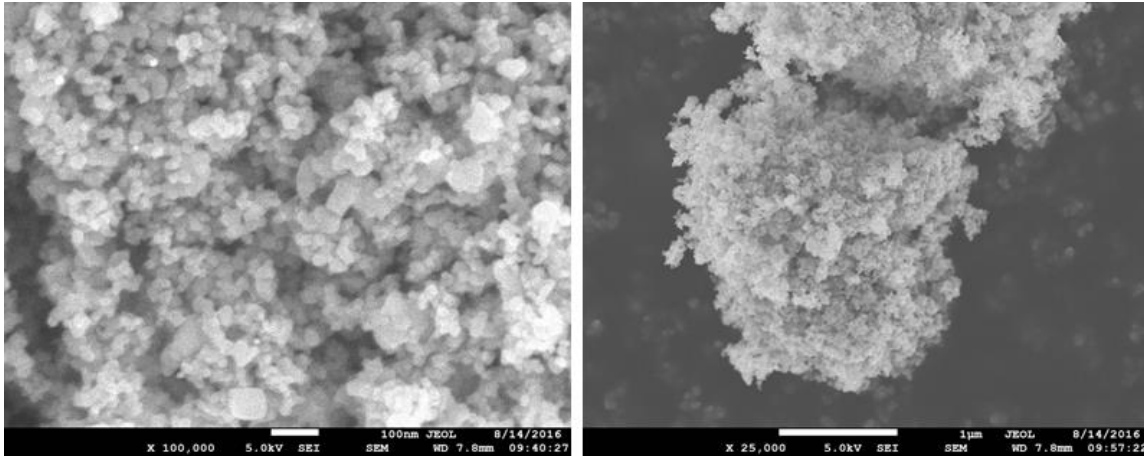
Figure 5 Scanning electron microscopy image of Au(20nm)/P25

UV-vis diffuse reflection spectra (Fig. 6) shows that pristine P25 barely absorb visible light with wavelength larger than 400 nm. Meanwhile, loading of Au NPs on P25 introduced plasmonic absorption peak of Au to the spectra, which extended the absorbing region of the photocatalyst to the visible range. The plasmonic absorption peak position differed among different Au NP sizes, i.e., 543nm/550nm/559nm for 10nm/20nm/30nm Au NPs. According to the literature [9], these wavelengths are ~20-30nm higher than the dipole mode plasmonic resonance peak of same size Au NPs in a vacuum, which is caused by the higher refractive index TiO_2 surrounding. Therefore, these absorption peaks are attributed to the plasmonic response of Au.
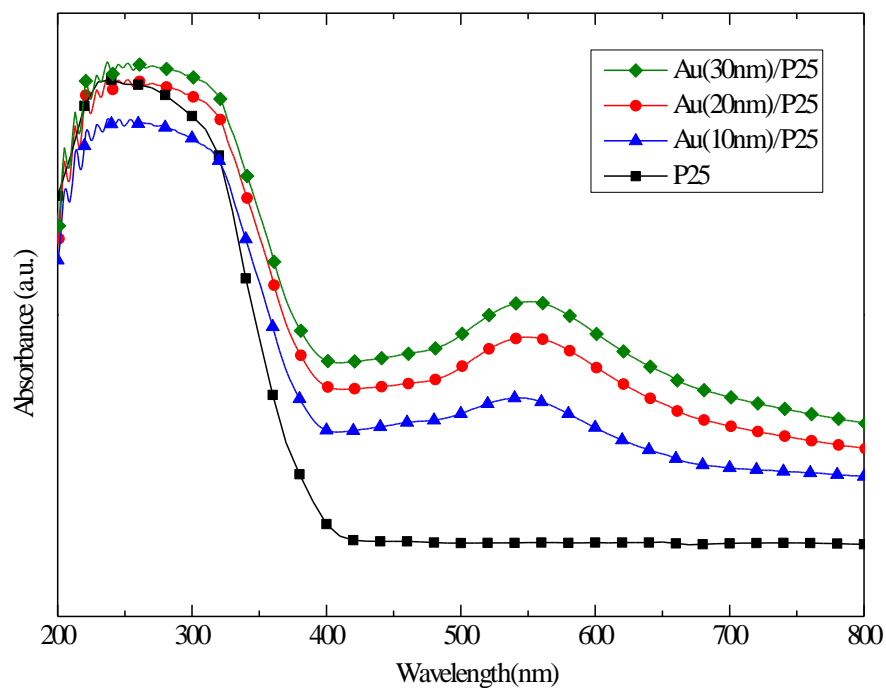
Figure 6 UV-vis diffuse reflection spectra pattern of P25, Au(10nm)/P25, Au(20nm)/P25, and Au(30nm)/P25

At the current stage, CO_2 photoreduction by water still has deficient activity. Therefore, for continuous flow reactor design, the signal detected by GC is also limited. Generally, for our CO_2 photoreduction experiments, the signal detected is ~10ppm for CO and ~1ppm for CH_4. Hence, to get a relatively accurate signal, it is vital to get rid of possible impurities/contamination. Argon tests were conducted for Au(20nm)/P25 sample to get rid of the influence of impurity on glass fiber filter. CO_2 reaction gas was switched to inert argon gas. For "filter calcined" group, we calcined the filter at 450°C for 2hrs right before loading it into the reaction chamber. For both calcined group and no-calcination control group, the reaction chambers were purged with argon gas for 12hrs to eliminate residual of CO_2 gas. According to the result shown in Fig. 7, no

significant CO/CH4 yield was observed for filter calcined group, while the control group produced a considerable amount of CO/CH4 under argon gas. Therefore, we claim that calcination of glass fiber filter is a necessary and sufficient pre-treatment for CO_2 photoreduction test, which will be applied for all the experiments below.
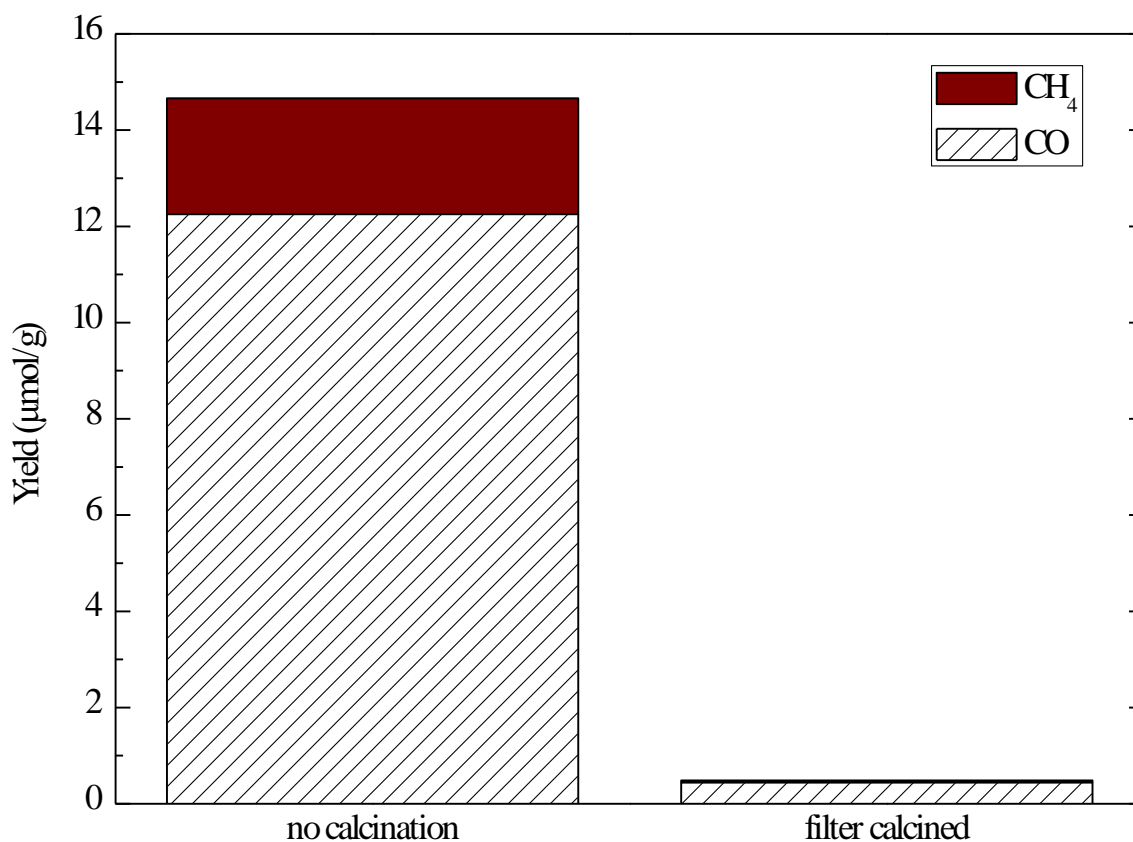

Figure 7 Argon gas test of Au(20nm)/P25

The visible light test was conducted to evaluate the effect of hot electron injection. A 435nm cut-off filter (Newport) was applied to the Xeon lamp. As photons

with wavelength larger than 435 nm are beyond the absorption edge of P25,

photoexcitation can only take place in Au NPs. Thus, visible light tests depict the hot

electron injection from Au NP to semiconductor conduction band. Results in Fig. 8 show

only CO is yielded (methane signals are not distinguishable from baseline), while

smaller size Au loaded catalyst showed higher activity comparing to larger size ones.

The work function of gold (5.4 eV) [25] and electron affinity of anatase-rutile mixed

phase TiO_2 (4.8 eV for rutile, 5.1 eV for anatase) [26] can be found in literature. The

Schottky Barrier Height (SBH) of Au/TiO_2 interface can, therefore, be evaluated with

Schottky-Mott rule to be ~0.6 eV for rutile phase and ~0.3 eV for anatase phase. 10nm

Au NPs theoretical have slightly larger work function[27] (~0.03eV larger than 30nm

NPs) which would increase SBH. Here we ignore this difference and assume all the gold

NPs have similar work functions. Therefore, Au/P25 structure should produce injection

of hot electron readily. However, for the visible light experiment, CO yield is much (2 to

4 orders of magnitude) lower than whole spectrum results (which we will show later),

indicating a low injection efficiency to TiO_2 CB. We will account for this in the

discussion.

  Notice the UV-vis results show higher visible light absorption for larger gold

NPs, we can deduce a more efficient damping of plasmon to hot electron and hot

electron injection to CB of TiO_2 in smaller size gold NPs. Hence, we attribute the

dramatically higher activity for small size gold NPs loaded catalyst in visible light

activity to the difference in the formation of hot carriers in Au NPs. This result is in

agreement with a theoretical prediction literature, which argued that smaller dimension

gold, in form of thin film, has higher probability of yielding hot electron through geometry-assisted intraband transition [28], while larger size gold NPs will form mostly hot holes. In consequence, direct injection of electron from gold NPs to TiO_2 is negatively related to the size of gold, while holds minor effect for whole spectrum activity.
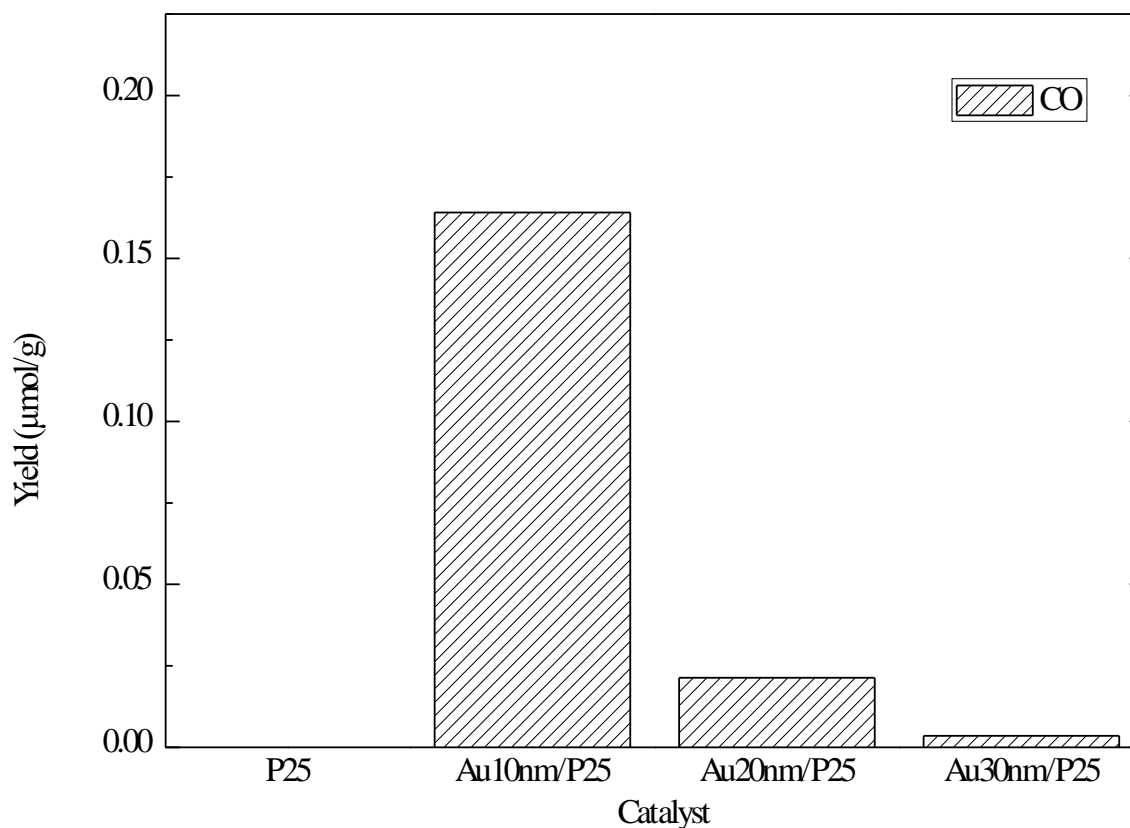

Figure 8 Visible light (435nm cut-off filter) photoactivity test

Al_2O_3 atomic layer deposition is introduced to unravel the role of Au NPs in CO2 photoreduction further. Before including gold NPs to the photocatalyst, P25 samples

with an Al_2O_3 surface coating but without gold NPs were tested for CO_2 reduction under Xeon lamp illumination. The results in Fig. 9 show that a thin coating of Al_2O_3 layers on P25 can improve the activity (optimum at 5 layers). This effect was attributed to the suppress of surface charge recombination[29, 30]. Namely, both anatase and rutile phase TiO_2 have an indirect band gap, which means the highest-energy state in the valence band has different momentum with the lowest-energy state in the conduction band. As interactions among different particles require the conservation of energy and momentum, this type of bandgap allows transition from VB to CB only with the assistant from lattice phonons. Similarly, for radiative recombination of carriers, which is the reverse process of photoexcitation, an assistant from lattice phonons are needed. Consequently, radiative recombination is not significant in TiO_2. In contrast, Shockley-Read-Hall (SRH) process, i.e., trap-assisted recombination, as well as surface recombination which has similar fundamental to SRH process, are predominant recombination processes in indirect band gap semiconductors. Hence, surface passivation by Al_2O_3 can reduce surface available trap states, therefore retard surface recombination on TiO_2 nanoparticles. Therefore, surface passivation effect is concluded to be responsible for the promotion effect of the Al_2O_3 interlayer coating. Five layers of the coating have a thickness of ~5Å, which is around the dimension of an anatase unit cell. Therefore, we can deduce one layer of coating cannot adequately cover the dangling bonds on the P25 surface for optimum surface passivation. When the layer becomes too thick, CO/CH_4 yield decreased, which is caused by the hindering of electron transport from interior P25 nanoparticle to surface adsorbed species on reaction center by a too thick Al_2O_3 layer.

17

Notably, five layers of coating also result in highest CH4 yield and selectivity. This consists with our reasoning above as surface passivation extended the lifetime of surface accumulated photoelectrons. Thereby, surface passivation effect also helps the formation of methane by a more significant amount of accumulated available photoelectron on photocatalyst surface.
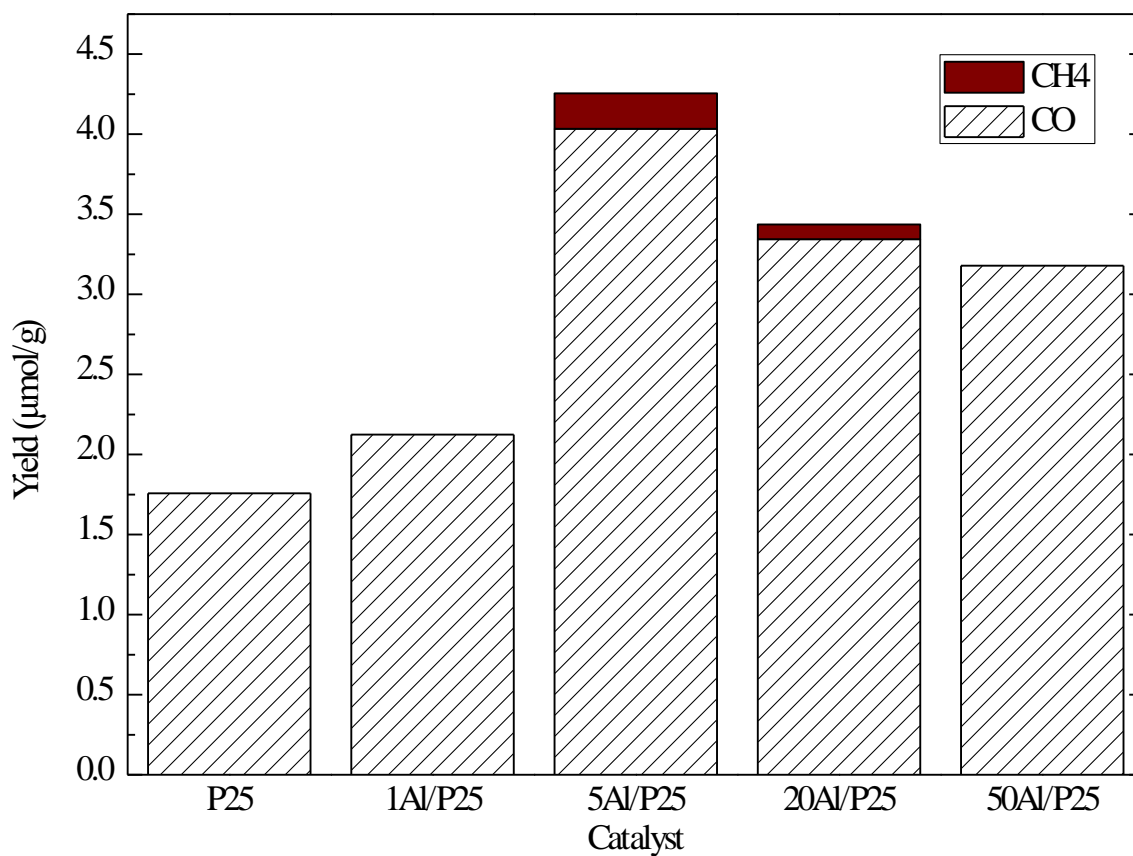

Figure 9 Whole spectrum CO$_2$ reduction activity of non-gold photocatalyst samples

CO$_2$ reduction activity of gold loaded photocatalysts are shown in Fig. 10 and

Tab. 1. CO and CH$_4$ are the main products for Au/Al$_2$O$_3$/TiO$_2$ photocatalyst, while CO

yield is an order of magnitude higher than CH$_4$. Overall yield is negatively related to the

PNPs dimension, namely 10nm PNPs loaded P25 showed the highest activity. It also

shows a similar relationship with the thickness of coating layer that thin coating of

aluminum oxide enhanced the photoactivity with an optimum coating thickness to be

~5Å. This trend is also explained as the combined effect of the suppress of surface

recombination and migration of electron from P25 to Au NPs through the Al$_2$O$_3$

layer[29], similar to the gold absent case. Comparing with results in Fig. 9, loading of

Au NPs induced enhancement for all the samples. The factor of enhancement reaches

maximum (~10 times) for Au10nm/5Al/P25 and decays to ~3 times for thick coating

samples.
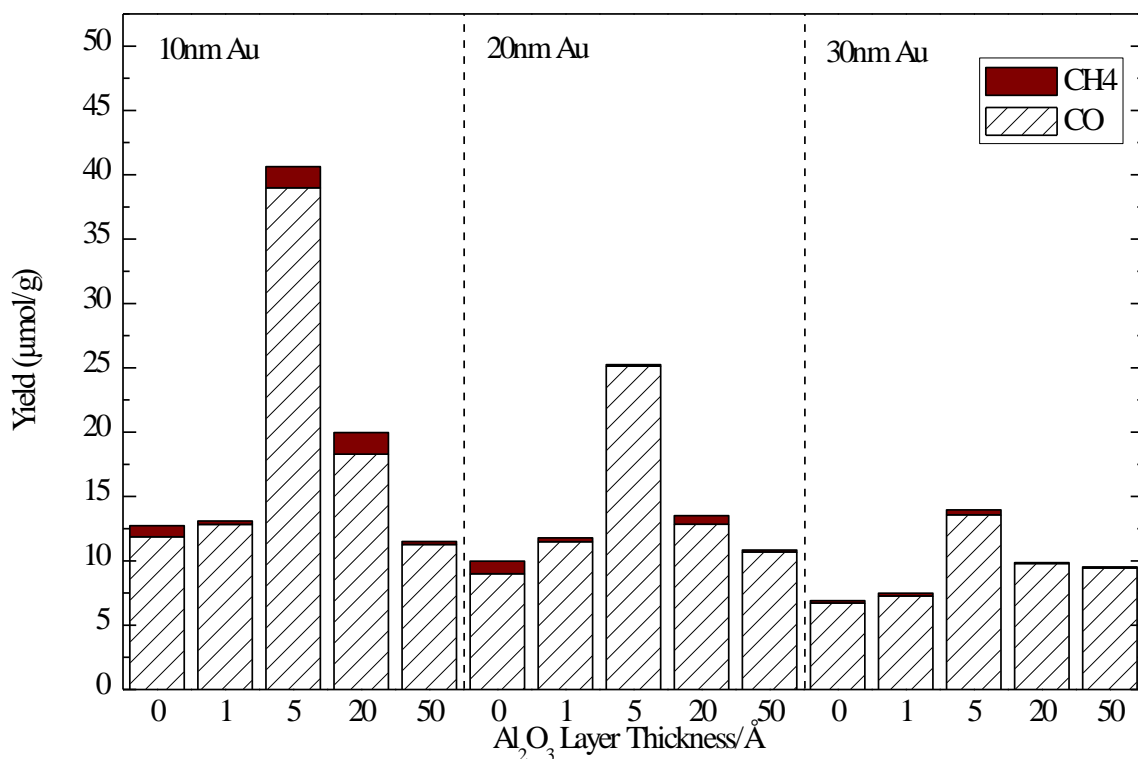
Figure 10 Whole spectrum CO_2 reduction activity of gold NPs loaded photocatalysts

Notably, comparing between different sizes of gold, smaller size gold NPs loaded photocatalysts showed higher overall activity and CH_4 selectivity, as shown in Fig. 11. Therefore, charge separation effect is likely playing a more critical role in Au/TiO_2 based catalysts for CO_2 reduction by water, as charge separation effect is well known to be more significant on smaller size gold NPs. In contrast, no significant correlation between selectivity and interlayer thickness was found.

Table 1 CO and CH$_4$ yield over 4 hrs illumination period

| Photocatalyst	CO yield/µmol·g^{-1}	CH$_4$ yield/µmol·g^{-1}
Au10nm/P25	11.86102	0.86699
Au10nm/1Al/P25	12.82209	0.2694
Au10nm/5Al/P25	38.99171	1.63938
Au10nm/20Al/P25	18.29452	1.67947
Au10nm/50Al/P25	11.27465	0.23091
Au20nm/P25	9.00214	0.96537
Au20nm/1Al/P25	11.48419	0.29506
Au20nm/5Al/P25	25.13265	0.11492
Au20nm/20Al/P25	12.85149	0.66708
Au20nm/50Al/P25	10.68294	0.16249
Au30nm/P25	6.72588	0.18094
Au30nm/1Al/P25	7.26735	0.2229
Au30nm/5Al/P25	13.58272	0.37336
Au30nm/20Al/P25	9.7967	0.06233
Au30nm/50Al/P25	9.43751	0.08729
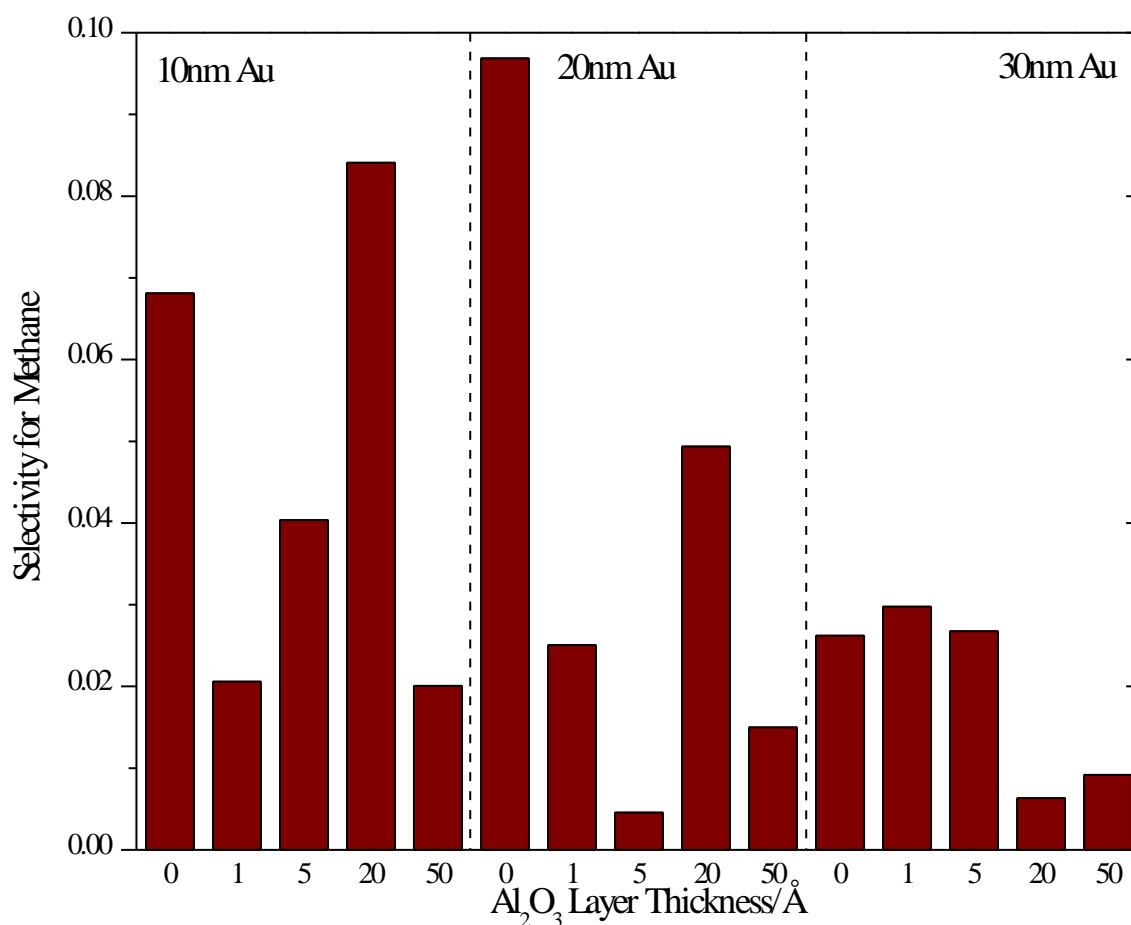
Figure 11 Selectivity for methane calculated from results in Figure 10

Although specific correlations were found, the contribution of near-field enhancement and charge separation is still not distinguished. To evaluate the role of near-field enhancement, FDTD simulation results are also included and will be discussed in the next chapter.

CHAPTER IV

SIMULATION RESULTS

Finite-difference time-domain (FDTD, Yee's method) simulation[31], which is a

time-domain finite difference method solving Maxwell's equation for modeling

computational electrodynamics, is included in order to investigate near-field

enhancement's effect and properties. In FDTD method, a Yee lattice is applied to

describe the E field and H field, in which each E vector component is located in the

center between a pair of H vector components, and vice versa. Furthermore, this method

also used a leapfrog scheme for matching the time of E field and H field updates. While

the nature of this method requires a limited small time-step to sustain simulation

stability, it also gets rid of the trouble to solve simultaneously updated equations.

In the study of this thesis, a commercial software Lumerical FDTD Solution is

used to conduct FDTD simulation. We first evaluated the resonant wavelength of Au

NPs by a reduced grid density simulation for all the configurations over 400~800nm

incident light. Optimum wavelength was found to be ~550nm for 20nm gold NPs in

contact with same size TiO_2 NP (within 540-560nm range for other sizes), which

consists with our UV-vis results and literature[32]. Therefore, we selected unitary

wavelength $\lambda = 550$nm as a light source for reducing simulation complexity. Total field

scattering field (TFSF) light source propagating along y^+ direction was used for all

simulation works. Here we present a comparison of different sizes of Au NPs

(10nm/20nm/30nm) loaded TiO_2 with different thickness of Al_2O_3 coating in order to evaluate the intensity of near-field enhancement under different conditions.

Simulated $/\mathbf{E}/^2$ results of different configurations are shown as the centerline *x-z* plane view of attached Au and TiO_2 nanospheres in Fig. 12-14. The color bar is scaled by the $\log_{10}$ value of $|\mathbf{E}|^2$. We can see that Au NPs show a strong response to the incident light and form high electric field in TiO_2 when the coating layer is absent. The maximum E^2 value is larger than 10000 times of incident light's E_0^2. Theoretically, this high electric field can induce a boosting of photoexcitation in TiO_2 based on Fermi's Golden rule. In contrast, with Al_2O_3 coating, we can see that the near-field enhancement is shielded by coating layers as it is confined in the vicinity of Au NPs. The enhanced field inside the TiO_2 particle is much smaller for 20 and 50 layers Al_2O_3 coated photocatalysts. Comparing among the different size of gold, we can find that for the configuration we considered, namely one gold nanoparticle attached to one semiconductor nanoparticle, larger size gold induced stronger field enhancement for its stronger plasmonic response.

Figure 12 FDTD result of $|E|^2$: x-z plane of 10nm diameter Au sphere (bottom) attached to 20nm diameter TiO$_2$ sphere (top) with different thickness of Al$_2$O$_3$ coating. Incident light wavelength = 550 nm.

Figure 13 FDTD result of $|E|^2$: x-z plane of 20nm diameter Au sphere (bottom) attached to 20nm diameter TiO$_2$ sphere (top) with different thickness of Al$_2$O$_3$ coating. Incident light wavelength = 550 nm.
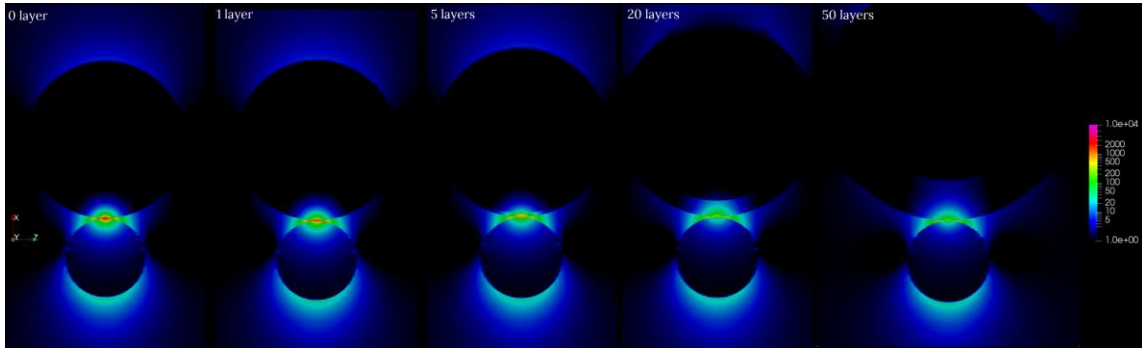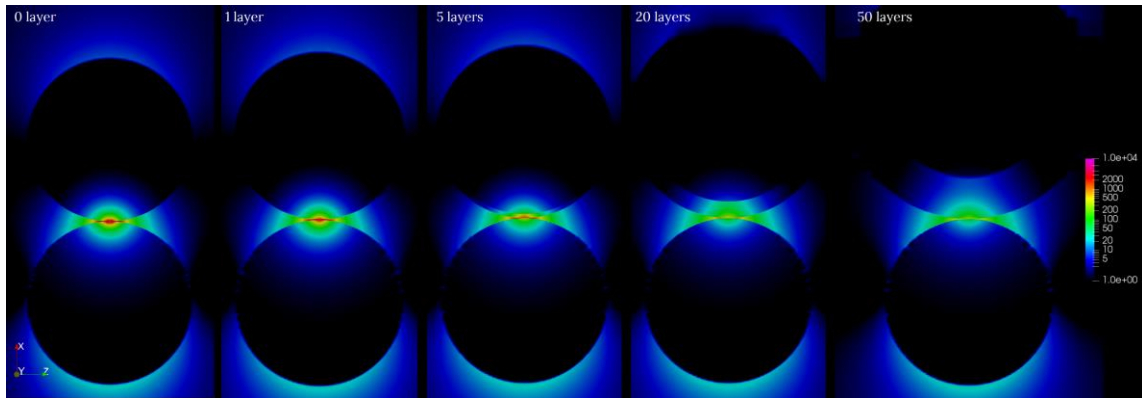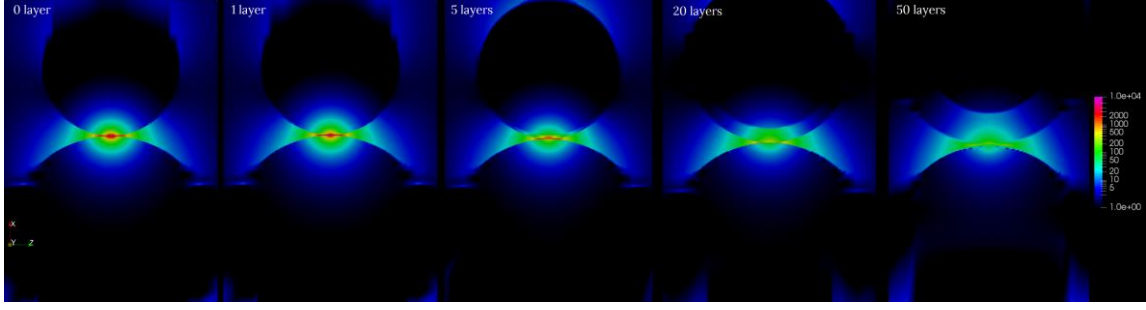
Figure 14 FDTD result of |E|^2: x-z plane of 30nm diameter Au sphere (bottom) attached to 20nm diameter TiO$_2$ sphere (top) with different thickness of Al$_2$O$_3$ coating. Incident light wavelength = 550 nm.

However, the conclusion we can get from the visualizations above are rather qualitative. In order to quantitatively understand the effect of near field enhancement, we calculated the overall field enhancement from FDTD data:

$$\mathbf{P} = \frac{\iiint w(x,y,z)|\mathbf{E}|^2 d\mathbf{V}}{\iiint w(x,y,z)|\mathbf{E_0}|^2 d\mathbf{V}}$$

in which *w(x,y,z)* is the weight function caused by recombination to depict a higher possibility for electron near the surface to reach TiO$_2$ surface, as shown in Fig. 15. Namely, electrons with a closer distance from the center of a nanosphere need to travel a longer distance and corresponding time to reach the surface. E$_0$ is the unit field strength induced by incident light. According to Fermi's Golden rule, the transition rate R$_{tran}$ induced by an incident light, which is considered as the perturbation term H', is proportional to the field intensity in the semiconductor region (from a statistic view neglecting the non-uniformity of semiconductor lattice), namely $R_{tran} \propto |\mathbf{E}|^2$. Therefore, the **P** value we calculated above describes the ratio of transition rate with the

presence of PNP attached to $Al_2O_3/TiO2$ nanoparticle to non-PNP attached nanoparticle. The python code for this calculation can be seen in Appendix I.
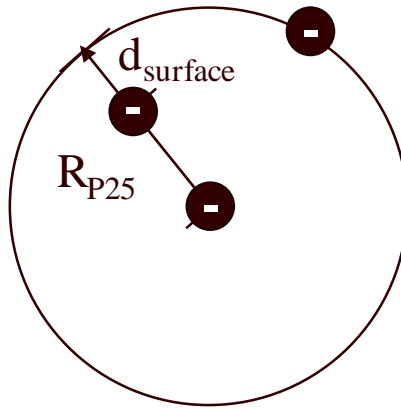
Figure 15 Illustration of origin of weight function w(r)

Fortunately, as the characteristic diffusion lengths of electrons and holes in both anatase and rutile TiO_2[33] exceed the dimension of P25 NPs, we can neglect the influence of recombination effect and set *w(x, y, z)* to be 1. The results of **P** are shown in Fig. 16. From the results we can find the effective field enhancement of a single Au NP to a single TiO_2 is around the magnitude of 10. Consisting with the visualization, larger size gold induced larger P value in TiO_2 region, while thicker Al_2O_3 interlayer shielded the near-field enhancement and cause P value to decrease.
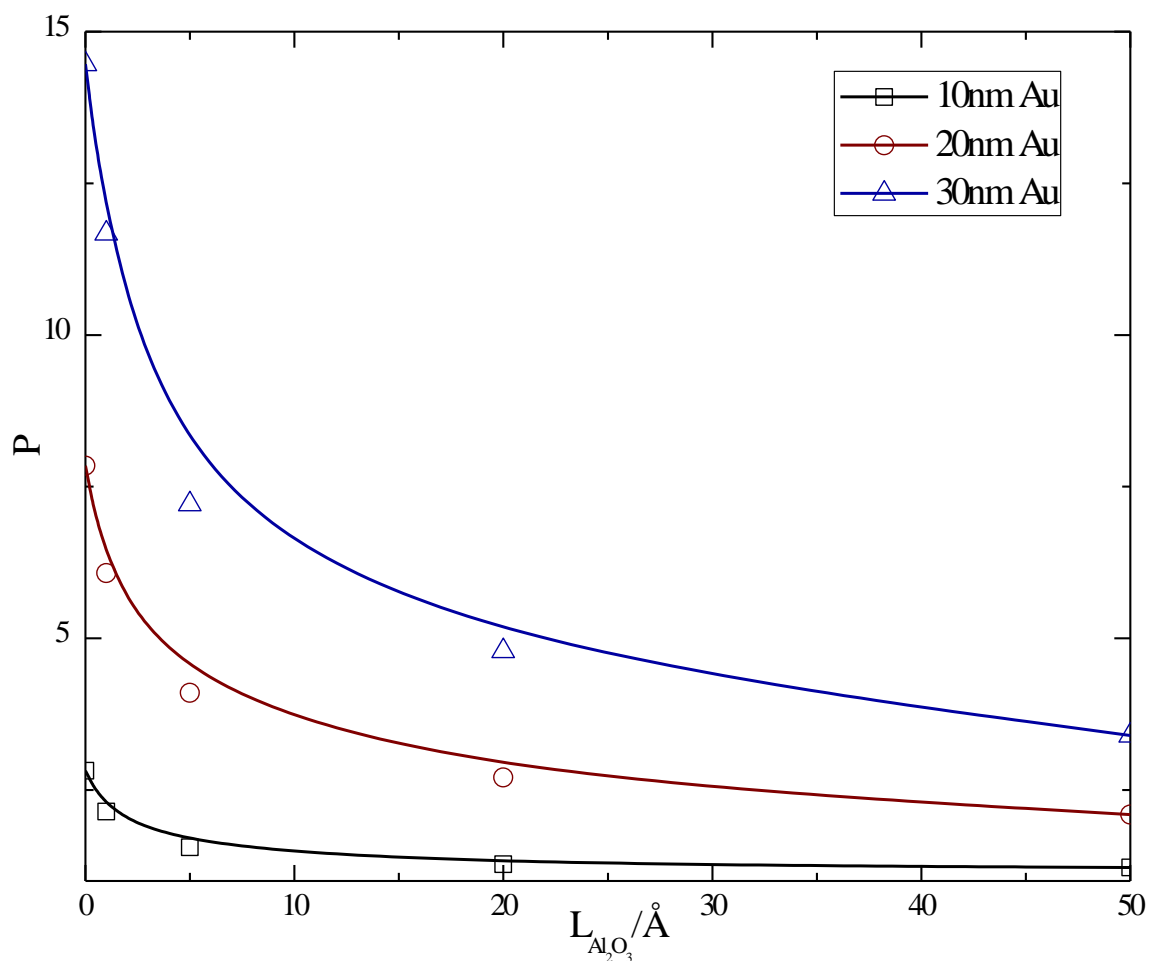
Figure 16 Calculated effective field enhancement of a single Au NP to attached TiO$_2$ nanosphere

Since we used only 0.5 wt.% of gold for our photocatalysts, the volume ratio between gold NPs and TiO$_2$ NPs would be ~0.001. Therefore, even for 10nm Au, assume a complete loading of gold NPs from suspension to TiO$_2$, the count ratio of Au to TiO$_2$ NPs will be less than 0.01. Furthermore, the bandgap of P25 is ~3eV, which is different from the resonant wavelength of Au NP. In another word, the **P** value we derived here is for the resonant frequency of PNPs. However, for a whole spectrum

illumination consisting of a different wavelength of photons, the averaged **P** value will

be smaller. Namely,

$$\mathbf{P}_{ave} = \frac{\int_\lambda \mathbf{P} \cdot f\ \lambda\ d\lambda}{\int_\lambda f\ \lambda\ d\lambda} < \mathbf{P}_{max}$$

in which $f(\lambda)$ is the intensity of light source corresponds to wavelength λ.

Therefore, the direct enhancement described by Fermi's Golden rule over the whole light

source spectrum is small and not capable of explaining for the high activity enhancement

with a coating layer (~10 times higher activity for 10nm Au on 0.5nm Al_2O_3 layer coated

TiO_2). Hence, direct near-field enhancement induced photo-excitation is most likely not

an important promotion effect in Au/TiO_2 structure.

Based on the small intrinsic Schottky barrier between Au and P25, we propose

that charge separation effect is still the governing effect in Au/TiO_2 system, which can

trap electrons in gold and retard the fast surface recombination, thereby extending the

lifetime of photoexcited carriers, especially photoexcited holes. LSPR induced strong

electric field in the vicinity of Au can help the charge separation process by changing it

from a spontaneous migration of carriers to a field guided transfer. Furthermore, with the

presence of Al_2O_3 interlayer, the LSPR of Au induced field can probably help electrons

to tunnel through the interlayer, as for angstrom length scale interlayer, the plasmonic

effect is also described in the quantum picture[34]. Furthermore, because hot electron

injection is rare for Au/P25 photocatalyst, which is in contrast with the intrinsic low

SBH between gold and P25, Fermi-leveling pinning effect is also considered. Fermi-

leveling pinning is caused by the surface dangling bonds and trap states, similar to

surface recombination. We suggest that the gold-P25 interface is pinned by surface trap states and therefore cause a high SBH hindering the hot electron injection. Introducing surface Al_2O_3 layer not only passivates surface state for lower surface recombination but eases Fermi-level pinning and results in lower SBH for carrier migration as well.

CHAPTER V

DISCUSSION AND CONCLUSION

In conclusion, $Au/Al_2O_3/P25$ hetero-structure with different Au size and Al_2O_3 layer thickness are synthesized and tested. Based on our experiments, simulation and analysis, charge separation (I) and hot electron injection (II) have a negative dependence on Au NPs size, while near-field enhancement (III) has a positive dependence on Au NPs size. From visible light activity test, hot electron injection is more significant with smaller gold size due to higher probability to form hot electron via intraband transition. Al_2O_3 coating can suppress surface charge recombination and electron transfer simultaneously. FDTD simulation and CO_2 reduction experiments show that ALD of Al_2O_3 will suppress the direct near-field enhanced photoexcitation significantly. Theoretical calculation estimated direct photoexcitation promotion by PNPs to be small for the weight ratio of Au we used. In contrast, we suggest LSPR induced field assisted charge separation effect will retain until the layer gets too thick, as shown in Fig. 17. Based on the above results and analysis, LSPR assisted charge separation is most likely the dominating mechanism for the enhancement of Au NPs to CO_2 photoreduction by water, while direct near-field enhancement promoted photoexcitation and hot electron injection hold minor effect.

31
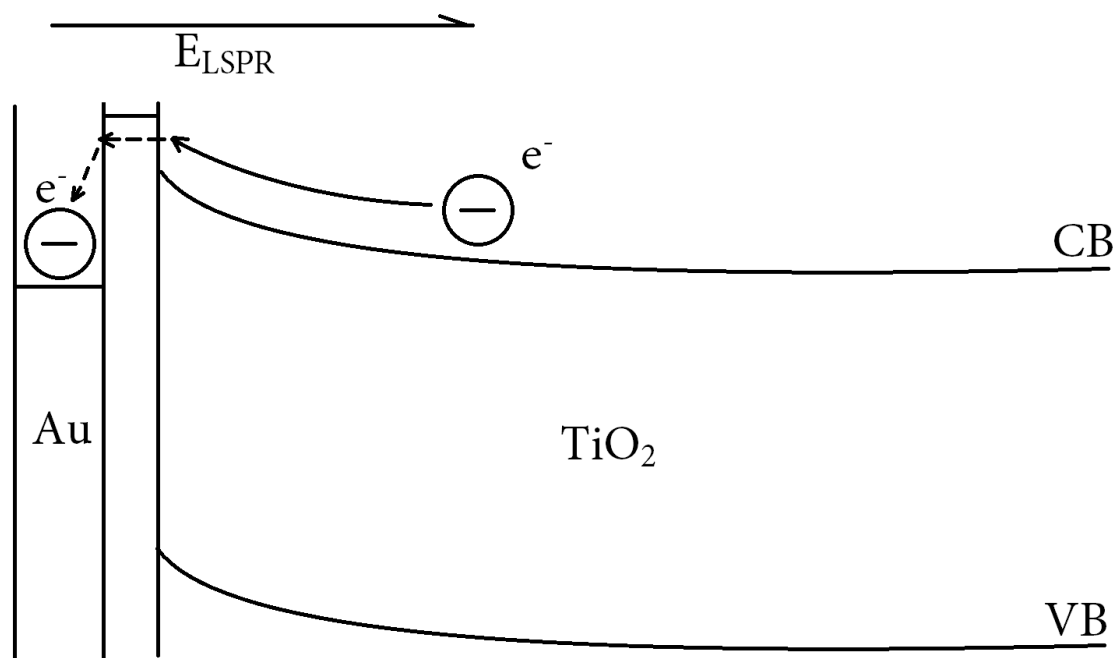
Figure 17 Illustration of LSPR assisted charge separation

Our results also show that, for TiO_2 based photocatalyst, smaller gold NPs are more favorable based on its stronger charge separation, hot electron generation capability and larger NPs count with fixed weight ratio. We also suggested that the low efficiency of hot electron injection is closely related to the surface trap states cause Fermi-level pinning. Hence, passivation of surface states is essential for improving photocatalytic activity. However, to further clarify the effect of plasmonic metals on CO_2 photoreduction on TiO_2, more future works, with emphasis on probing or first principle based simulation of surface states, are urged.

REFERENCES

1. Cox, P.M., et al., *Acceleration of global warming due to carbon-cycle feedbacks in a coupled climate model.* Nature, 2000. **408**(6809): p. 184.

2. Habisreutinger, S.N., L. Schmidt-Mende, and J.K. Stolarczyk, *Photocatalytic Reduction of CO_2 on TiO_2 and Other Semiconductors.* Angewandte Chemie International Edition, 2013. **52**(29): p. 7372-7408.

3. Koci, K., et al., *Effect of silver doping on the TiO_2 for photocatalytic reduction of CO_2.* Applied Catalysis B-Environmental, 2010. **96**(3-4): p. 239-244.

4. Li, Y., et al., *Photocatalytic reduction of CO_2 with H_2O on mesoporous silica supported Cu/TiO_2 catalysts.* Applied Catalysis B: Environmental, 2010. **100**(1–2): p. 386-392.

5. Kočí, K., L. Obalová, and Z. Lacný, *Photocatalytic reduction of CO_2 over TiO_2 based catalysts.* Chemical Papers, 2008. **62**(1): p. 1-9.

6. Liu, L. and Y. Li, *Understanding the reaction mechanism of photocatalytic reduction of CO_2 with H_2O on TiO_2-based photocatalysts: a review.* Aerosol Air Qual Res, 2014. **14**(2): p. 453-469.

7. Fujishima, A. and K. Honda, *Electrochemical photolysis of water at a semiconductor electrode.* Nature, 1972. **238**(5358): p. 37-38.

8. Wang, C., et al., *Visible light photoreduction of CO_2 using $CdSe/Pt/TiO_2$ heterostructured catalysts.* The Journal of Physical Chemistry Letters, 2009. **1**(1): p. 48-53.

9.   Xuming, Z., et al., *Plasmonic photocatalysis.* Reports on Progress in Physics, 2013. **76**(4): p. 046401.

10.   Subramanian, V., E.E. Wolf, and P.V. Kamat, *Catalysis with TiO₂/gold nanocomposites. Effect of metal particle size on the Fermi level equilibration.* Journal of the American Chemical Society, 2004. **126**(15): p. 4943-4950.

11.   Yui, T., et al., *Photochemical reduction of CO₂ using TiO₂: effects of organic adsorbates on TiO₂ and deposition of Pd onto TiO₂.* ACS applied materials & interfaces, 2011. **3**(7): p. 2594-2600.

12.   Jakob, M., H. Levanon, and P.V. Kamat, *Charge distribution between UV-irradiated TiO2 and gold nanoparticles: determination of shift in the Fermi level.* Nano Letters, 2003. **3**(3): p. 353-358.

13.   Rycenga, M., et al., *Controlling the synthesis and assembly of silver nanostructures for plasmonic applications.* Chemical Reviews, 2011. **111**(6): p. 3669-3712.

14.   Clavero, C., *Plasmon-induced hot-electron generation at nanoparticle/metal-oxide interfaces for photovoltaic and photocatalytic devices.* Nature Photonics, 2014. **8**(2): p. 95-103.

15.   Cushing, S.K., et al., *Photocatalytic activity enhanced by plasmonic resonant energy transfer from metal to semiconductor.* Journal of the American Chemical Society, 2012. **134**(36): p. 15033-15041.

16.   Li, J., et al., *Plasmon-induced resonance energy transfer for solar energy conversion.* Nature Photonics, 2015. **9**(9): p. 601-607.

17.   Hou, W., et al., *Photocatalytic conversion of CO_2 to hydrocarbon fuels via plasmon-enhanced absorption and metallic interband transitions.* Acs Catalysis, 2011. **1**(8): p. 929-936.

18.   Tu, W., et al., *Au@ TiO_2 yolk–shell hollow spheres for plasmon-induced photocatalytic reduction of CO_2 to solar fuel via a local electromagnetic field.* Nanoscale, 2015. **7**(34): p. 14232-14236.

19.   Kar, P., et al., *Enhanced CH_4 yield by photocatalytic CO_2 reduction using TiO_2 nanotube arrays grafted with Au, Ru, and ZnPd nanoparticles.* Nano Research, 2016. **9**(11): p. 3478-3493.

20.   Ji, X., et al., *Size control of gold nanocrystals in citrate reduction: the third role of citrate.* Journal of the American Chemical Society, 2007. **129**(45): p. 13939-13948.

21.   Zhao, H., et al., *Enhancing photocatalytic CO_2 reduction by coating an ultrathin Al_2O_3 layer on oxygen deficient TiO_2 nanorods through atomic layer deposition.* Applied Surface Science, 2017. **404**: p. 49-56.

22.   Tanaka, A., et al., *Preparation of Au/TiO_2 with metal cocatalysts exhibiting strong surface plasmon resonance effective for photoinduced hydrogen formation under irradiation of visible light.* Acs Catalysis, 2012. **3**(1): p. 79-85.

23.   Jovic, V., et al., *Effect of gold loading and TiO_2 support composition on the activity of Au/TiO_2 photocatalysts for H_2 production from ethanol–water mixtures.* Journal of Catalysis, 2013. **305**: p. 307-317.

24.   Chan, S.C. and M.A. Barteau, *Preparation of highly uniform Ag/TiO$_2$ and Au/TiO$_2$ supported nanoparticle catalysts by photodeposition.* Langmuir, 2005. **21**(12): p. 5588-5595.

25.   Haynes, W.M., *CRC handbook of chemistry and physics*. 2014: CRC press.

26.   Scanlon, D.O., et al., *Band alignment of rutile and anatase TiO$_2$.* Nature materials, 2013. **12**(9): p. 798-801.

27.   Wood, D.M., *Classical size dependence of the work function of small metallic spheres.* Physical Review Letters, 1981. **46**(11): p. 749.

28.   Sundararaman, R., et al., *Theoretical predictions for hot-carrier generation from surface plasmon decay.* Nature communications, 2014. **5**.

29.   Kim, W., et al., *Photocatalysis of dye-sensitized TiO$_2$ nanoparticles with thin overcoat of Al$_2$O$_3$: enhanced activity for H$_2$ production and dechlorination of CCl$_4$.* The Journal of Physical Chemistry C, 2009. **113**(24): p. 10603-10609.

30.   Prasittichai, C. and J.T. Hupp, *Surface modification of SnO$_2$ photoelectrodes in dye-sensitized solar cells: significant improvements in photovoltage via Al$_2$O$_3$ atomic layer deposition.* The Journal of Physical Chemistry Letters, 2010. **1**(10): p. 1611-1615.

31.   Yee, K., *Numerical solution of initial boundary value problems involving Maxwell's equations in isotropic media.* IEEE Transactions on antennas and propagation, 1966. **14**(3): p. 302-307.

32.   Jain, P.K., et al., *Calculated absorption and scattering properties of gold nanoparticles of different size, shape, and composition: applications in*

biological imaging and biomedicine. J. Phys. Chem. B, 2006. **110**(14): p. 7238-7248.

33.   Yamada, Y. and Y. Kanemitsu, *Determination of electron and hole lifetimes of rutile and anatase TiO$_2$ single crystals.* Applied Physics Letters, 2012. **101**(13): p. 133907.

34.   Savage, K.J., et al., *Revealing the quantum regime in tunnelling plasmonics.* Nature, 2012. **491**(7425): p. 574-577.

APPENDIX I

PYTHON CODE FOR P FACTOR CALCULATION

```
#This code performs integration of E^2 for given data set of E^2
corresponding to x, y, z data sets and TiO2 center location.
#import E^2, x, y, z data from csv files

import numpy as np
E_2 = np.loadtxt(open("0.txt","rb"),delimiter=",",skiprows=0)
x = np.loadtxt(open("0.x.txt","rb"),delimiter=",",skiprows=0)
y = np.loadtxt(open("0.y.txt","rb"),delimiter=",",skiprows=0)
z = np.loadtxt(open("0.z.txt","rb"),delimiter=",",skiprows=0)

#Define data array length

x_len = len(x)
y_len = len(y)
z_len = len(z)
V_sigma = 0
E_2_V = 0

print("E_2 array size =", len(E_2))

o_gold = [2e-8,1e-8,1e-8]
r_gold = 1e-8 #set the radius and center position of TiO2 NP

#Perform integration for E^2

for i in range(x_len-1):
    for j in range(y_len-1):
        for k in range(z_len-1):
            if (x[i+1]-o_gold[0])**2 + (y[j+1]-o_gold[1])**2 +
(z[k+1]-o_gold[2])**2 <= r_gold**2:
                V_delta = (x[i+1]-x[i])*(y[j+1]-y[j])*(z[k+1]-
z[k])
                V_sigma += V_delta
                E_2_V +=
1/8*(E_2[(k+1)*x_len*y_len+(j+1)*x_len+i+1] +
E_2[(k)*x_len*y_len+(j)*x_len+i] +
E_2[(k+1)*x_len*y_len+(j+1)*x_len+i] +
E_2[(k+1)*x_len*y_len+(j)*x_len+i] +
E_2[k*x_len*y_len+j*x_len+i+1] +
```

```
E_2[k*x_len*y_len+(j+1)*x_len+i+1] +
E_2[(k+1)*x_len*y_len+j*x_len+i+1] +
E_2[k*x_len*y_len+(j+1)*x_len+i])*V_delta

#Calculate E^2 average value

E_2_ave = E_2_V/V_sigma

print("V_sigma =", V_sigma, "E_2_V =", E_2_V, "E_2_ave =",
E_2_ave, end=' ')
```